RESEARCH ARTICLE

NANO · MICRO small
www.small-journal.com

Evolution of Curvatures Between Lamellar and Bicontinuous Phases: Formation of Saddle-Shaped Hierarchical Lamellar Structures in Binary Self-Assembly System

Shuqi Wang, Ya Li, Bin Yang, Hao Chen, Lu Han, Yuanyuan Cao,* and Yongsheng Li**

Curvatures are fundamental parameters governing the topological changes and phase separations in soft matter systems. Explorations of Gaussian curvature, mean curvature, and their combination (as interfacial curvature linked to packing parameter) are essential for understanding the dynamic self-assembly processes, especially for the critical and classic lamellar-to-bicontinuous transition. However, whether intermediate states arising from the changes in these curvatures exist remains a long-standing controversy. Herein, this issue is addressed by identifying a unique saddle-shaped hierarchical lamellar phase in a binary self-assembly system containing polystyrene-*b*-poly(acrylic acid) (PS-*b*-PAA) and stearyltrimethylammonium bromide (STAB). This intermediate phase exhibits characteristics with negative Gaussian curvature similar to bicontinuous phase while maintaining lamellar topologies. Its existence attributes to the competing effects of the inserted STAB micelles imposed on PAA segments: electrostatic screening reduces PAA effective volume, while volume expansion increases it. This competition balance promotes the lamellae toward saddle-shapes with enhanced molecular capacity and modulates their interfacial curvature to a critical intermediate value that is rarely stable in block copolymer systems. The thermostability of this intermediate phase serves as compelling evidence for the smooth interfacial curvature evolution pathway. This discovery provides insights into phase transformations in biological membranes, marking a significant advance in understanding complex soft matter systems.

1. Introduction

As a fundamental property of geometry, curvature defines how curves deviate from straightness and how surfaces deviate from planarity.[1] Mathematicians have developed a series of curvature concepts to describe the geometries ranging from macroscopic objects to microscopic entities. For example, Gaussian curvature, defined as the product of the two principal curvatures at a point on a given surface, and mean curvature, which is the average of the principal curvatures, have been extensively employed as the intrinsic determination of surface geometries.[2,3] Distinct Gaussian curvatures differentiate divergent geometries with markedly different topologies, configurations, and properties. The positive Gaussian curvatures correspond to the spherical and elliptic shapes, and the zero Gaussian curvature represents the Euclidean shapes (e.g., the planes and the cylinders).[3] Specifically, the unique negative Gaussian curvature describes saddle-shaped geometry as doubly curved hyperbolic surfaces with opposing principal curvatures, which is well-known as the typical feature of the bicontinuous cubic structures that feature triply periodic minimal surfaces with zero mean curvature everywhere.[4] The negative Gaussian curvature values have endowed this shape with kinds of intriguing properties such as exceptional mechanical resilience, efficient load-bearing,[5,6] light manipulation and catalytic capabilities,[7–10] exhibiting adaptive functional performances in diverse biological and environmental contexts.[11,12]

Curvatures are also significant geometrical parameters concern the behaviors and properties of matter in the microscopic world.[13–15] For instance, for self-assembled amphiphiles (such as surfactants, lipids, or block copolymers), the geometry of the molecular aggregates (such as micelles) can typically be described by their effective packing into various interfacial curvatures at the hydrophilic/hydrophobic interface.[3,16,17] The interfacial curvature plays significant roles in determining mesoscopic organizations and ultimately governing the topological morphology of the final macroscopic structures. This interfacial curvature is the combination of Gaussian curvature and mean curvature, arising from a spontaneous process governed by the amphiphile

S. Wang, Y. Li, B. Yang, Y. Cao, Y. Li
Lab of Low-Dimensional Materials Chemistry
Key Laboratory for Ultrafine Materials of the Ministry of Education
Frontiers Science Center for Materiobiology and Dynamic Chemistry
Shanghai Engineering Research Center of Hierarchical Nanomaterials
School of Materials Science and Engineering
East China University of Science and Technology
Shanghai 200237, China
E-mail: yuanyuancao@ecust.edu.cn; ysli@ecust.edu.cn
H. Chen
Institute of Mathematical Sciences
ShanghaiTech University
393 Middle Huaxia Road, Shanghai 201210, China
L. Han
School of Chemical Science and Engineering
Tongji University
1239 Siping Road, Shanghai 200092, China
E-mail: luhan@tongji.edu.cn
The ORCID identification number(s) for the author(s) of this article can be found under https://doi.org/10.1002/smll.202508085

DOI: 10.1002/smll.202508085

packing parameter $p = V/a_0 l$, where V is the hydrophobic chain volume, a_0 is the effective area of the hydrophilic head group, and l is the dynamical hydrophobic chain length.[16,17] When the head-to-tail volume ratio of molecules is altered, the interfacial curvature undergoes quantitative adjustments, thereby driving structural transitions between distinct topological phases.[18,19] This phenomenon can be also explained by the Helfrich curvature elastic free energy theory, which provides a theoretical framework for predicting phase transition pathways from the energy perspective.[20]

Therefore, clarifying the dynamics of evolution of various curvatures in self-assembly systems not only establishes theoretical models for understanding the essence of self-assembly, enabling precisely correlating the microscale molecular geometries with mesoscale topological architectures, but also provides a foundational framework for the rational design of novel functional materials. For amphiphilic assemblies, with the evolution of the interfacial curvatures (along with the p parameter decrease from 1 to 2/3), the system undergoes a lamellar to bicontinuous phase transition. This is a classic and fundamental phenomenon with significant restructured topological structures and geometric experiences (i.e., the Gaussian curvatures of the assemblies evolute from zero to negative), which is particularly important as it is directly related to the critical cell membrane transformations in biology, the topological reconstruction of self-morphing engineering, and the property evolution in artificially membrane materials.[12,21–25] However, a critical question about the evolution of different curvatures in this kind of phase transition has long remaining unanswered: there lacks a smooth geometric transition path with continuous structural deformation to explain such remarkable and abrupt Gaussian curvature changes, or whether there is a saddle-shaped intermediate lamellar phase with negative Gaussian curvature and zero mean curvature, i.e., not only preserves the essential characteristics of the lamellar phase but also exhibits the minimal surface features of the bicontinuous phase, that effectively correlates the two phases. Since the saddle-like lamellae was long been considered as a thermodynamically unstable phase that have never been found in traditional surfactant or block copolymer assembly systems, the problem to capture or to achieve such non-Euclidean geometric structure through component design remains an open challenge in the field.

Block copolymers are ideal building blocks for generating ordered structures owing to their highly tunable and versatile compositions.[26] Unlike the well-established microphase separation in melt states, their self-assembly behavior in solution is much more complex, which could access to more intricate structural transitions.[27,28] The tetrahydrofuran (THF)/water mixture system provides a typical solution environment for self-assembly, where THF serves as a good solvent for most hydrophobic or weakly polar blocks, whereas water is compatible with hydrophilic segments. Polymer–polymer and polymer–solvent interactions play crucial roles in driving the assembly of the polymer, so that the structural transitions can be well controlled through various strategies.[10,26,29] Therefore, the self-assembly of block copolymers in THF/water solution has provides a robust and versatile platform for investigating structural transitions and the evolution of different curvatures.

Herein, we report the formation and structural transition of thermodynamically stable pupa-like lamellar silica nanoparticles, characterized by a saddle-shaped lamellar phase with secondary multilayer structures (saddle-SML) via a binary self-assembly system containing a block copolymer polystyrene-*b*-poly (acrylic acid) (PS-*b*-PAA) as the main building block and a small molecule surfactant stearyltrimethylammonium bromide (STAB) as the structural modulator. The interactions between the two components, i.e., the charge complementarity between the cationic head of the surfactant and the anionic PAA chains, and the hydrophobic interactions between the nonpolar tails of STAB and the hydrophobic PS segment, induced the insertion of STAB within the polymer microdomains that impacted competition effects on the effective volume fractions of the polymer. This competition regulated the binary assembly behaviors with exceptional flexibility and versatility that are richer than that of the sole amphiphiles. As a consequence, an unbalanced hierarchical saddle-like lamellar phase with two set of size-distinct pore arrangements (that is, the primary pores and the secondary subpores) has appeared between the lamellar and bicontiunous phases by modulating the relative ratios of the two components. The Gaussian curvature and mean curvature characteristics of these phases were analyzed and assessed through the reconstructed model using electron tomography (ET). Meanwhile, their secondary multilayer structures with different number of layers (ranging from 1 to 4) templated by the inserted STAB micelles can be conveniently and efficiently adjusted within their phase region. Through thoroughly investigated the formation mechanism of saddle-SML by exploring the relationship between the synthesis conditions (the ratio of two components and the length of the block copolymer) and the structure parameters, the importance of the interfacial curvature matching effect in influencing the phase behaviors of the assembly system have been revealed.

2. Results and Discussion

2.1. Synthesis and Characterization of Saddle-SML

Our binary system is based on the cooperative self-assembly between the anionic block copolymer PS_{92}-*b*-PAA_{16} (as reported previously[30]) and the cationic surfactant STAB, depending on the electrostatic attraction between their polar heads and the hydrophobic interactions between their hydrophobic parts. The co-assembly process was initiated by poor solvent-induced self-assembly, during which the THF solution of the polymers was poured into a dense aqueous solution of the surfactant, followed by a silica replicating process to *frozen* the assemblies. Under a STAB/PS_{92}-*b*-PAA_{16} molar ratio of 382.2:4.6 (mass ratio of 150:50), pupa-like composite micelles with axially stacked lamellar structure were formed (**Figure 1a**). The PAA lamellar segments of the micelles were stained to distinguish the positions of each polymer blocks, where a typical alternating lamellar arrangement with ≈8 nm space apart was revealed, corresponding to the volume of the PS segments. The micelles were sequentially precisely biomineralized *in-situ* via the sequential deposition and calcination of silica source tetraethyl orthosilicate (TEOS) to obtain a stable and rigid structure. The structures were characterized by the small angle X-ray scattering (SAXS) measurements (Figure 1g) and the reflections with q value of 0.035, 0.069, and

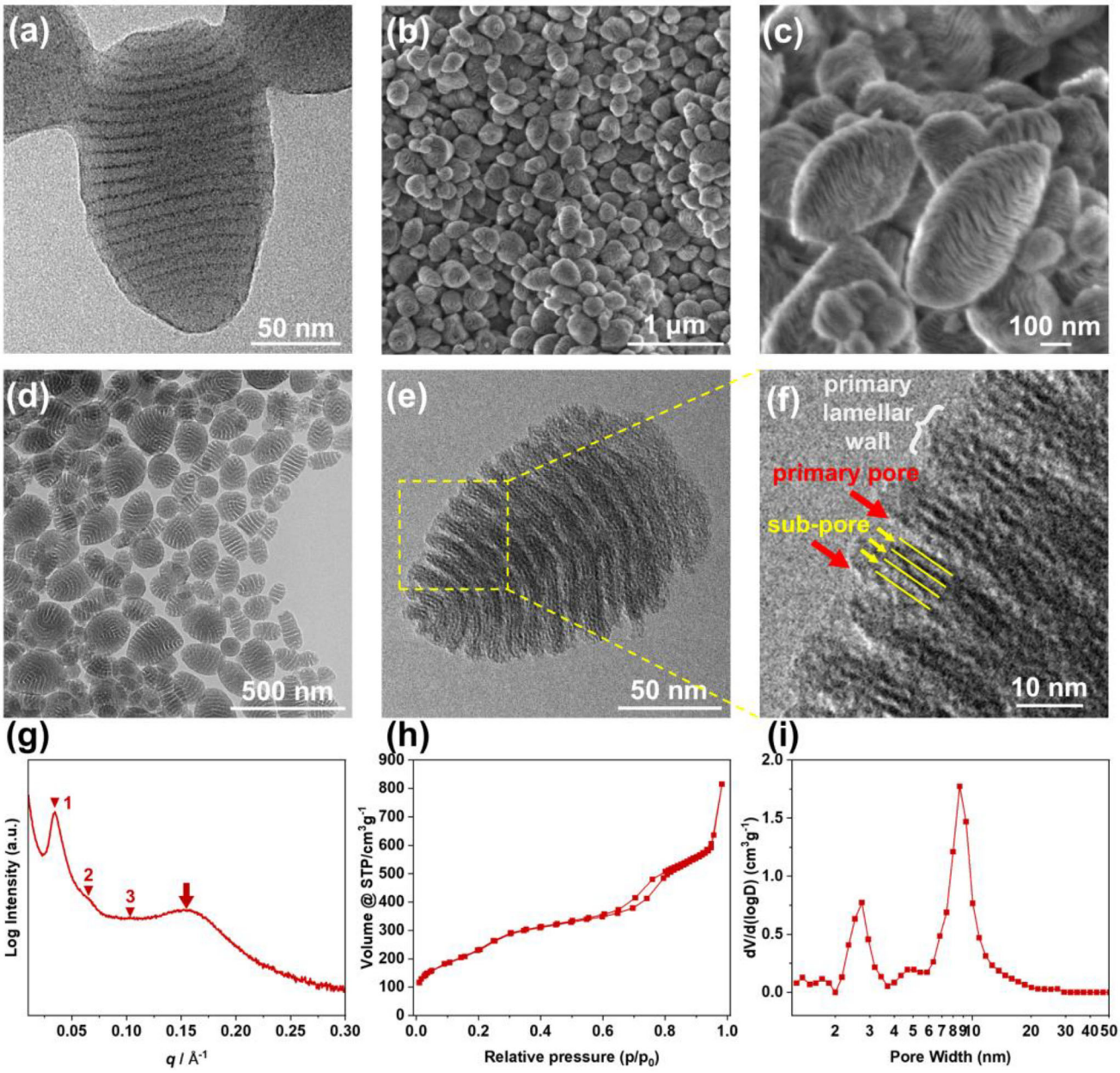

Figure 1. a) TEM images of the composite micelles synthesized by the co-assembly of STAB/PS_{92}-*b*-PAA_{16} with molar ratios of 382.2:4.6. b) Low-magnified and c) high-magnified SEM images of the saddle-SML nanoparticles obtained in synthesis conditions with molar ratio of STAB/PS_{92}-*b*-PAA_{16}/TEOS equals to 382.2:4.6:720.0, d) Low-magnified and e,f) high-magnified TEM images of the saddle-SML nanoparticles. g) SAXS pattern and h) N_2 adsorption-desorption isotherms of the saddle-SML nanoparticles. i) Pore size distribution calculated from the adsorption branch of the N_2 sorption isotherms by Non-Local Density Functional Theory (NLDFT) method.

0.107 $Å^{-1}$ were indexed to the 1st, 2nd and 3rd order reflections, respectively, conforming to the character of a lamellar scattering feature: d_1:d_2:d_3 = 1:1/2:1/3. The broad scattering peak at 0.154 $Å^{-1}$ may suggest the presence of the secondary periodic subpores with a spacing calculated ≈4 nm (as shown by the red arrow in Figure 1g). The materials exhibited uniform pupa-like morphology with a long axis of ≈290 nm and a short axis of ≈190 nm from scanning electron microscopy (SEM) observation (Figure 1b,c), corresponding to an average particle size of 255 nm as measured by dynamic light scattering (DLS) experiment (Figure S1, Supporting Information). Notably, the pupa-like nanoparticles were featured by curved lamellar patterns on the external surfaces, implied an unusual lamellar deformation. The corresponding inner structural details of the nanoparticles were revealed via transmission electron microscopy (TEM, Figure 1d–f), which exhibited a hierarchical curved lamellar structure with large open pores (≈6.5 nm, marked by red arrow) and 3-slit pores (slit width ≈2 nm, marked by yellow

arrows) sandwiched between four silica sublayers (marked by yellow lines) as magnified in Figure 1f. We then termed the hierarchical structure of this pupa-like nanoparticle as SML (the lamellar stacked phase with secondary multilayer structures) and referred to the large lamellae as primary lamellar walls (indicated by white bracket) and large interlayer space as primary pores (indicated by red arrows), while small slits inserted in the primary lamellar walls were referred as subpores (indicated by yellow arrows), respectively. The hierarchical pores were further characterized by N_2 adsorption-desorption isotherms, in which a combined H2- and H4-type hysteresis loops indicated the presence of both channel–type mesopores with 8.6 nm width and narrow slit-type mesopores with 2.7 nm width (Figure 1h,i).

2.2. Structural Solution and Evaluation of Gaussian and Mean Curvatures

Interestingly, we found that the projection characteristics of the nanoparticles at specific TEM observation angles showed exceptional overlapping contrast, resembling superposed projections of two batches of curved surfaces bending toward opposite directions (**Figure** 2b$_2$). This phenomenon was particularly evident when the particles were observed by rotating along their long axis (Figure 2b; Figure S2, Supporting Information). During the rotation of the nanoparticle, the TEM contrast of the lamellar structure transitioned sequentially from downward to crossed and finally to upward orientations (the lamellae are indicated by the yellow dashed line in Figure 2b). These opposing lamellar directions indicated that these nanoparticles were intrinsically composed of exceptional saddle-shaped lamellar surfaces with opposite principal curvatures at orthogonal directions, as modeled in the upright corner of each TEM image (therefore we termed this nanoparticles as saddle-SML), rather than the typical elliptic or parabolic surfaces commonly observed in traditional block copolymer microphase separation systems (Figure 2a).[18,31] To clarify, we employed ET to restore the 3D volumetric information of the nanoparticles from a series of 2D TEM projections taken at various angles.[32,33] A tilt series of 21 TEM images tilting from −60° to +60° along the long axis of the particles were taken at an interval of 5° and the 3D volume was reconstructed by real-space iterative reconstruction (RESIRE) algorithm.[34,35] The reconstructed tomogram of a typical saddle-SML particle is presented in Figure 2c, which exhibits projection features comparable to those observed in TEM images (Figure 2b), and the corresponding complete tilt series of TEM images are presented in Figure S2 (Supporting Information). The reconstructed tomogram can be visualized from cross-sectional slices, enabling comprehensive observations of the internal architectures. The cross-sections along rotating the central longitudinal axis in Figure 2d (the corresponding complete cross-sections series are shown in Figure S3, Supporting Information; 18° intervals), along with parallel longitudinal sections at varying depths (≈10 nm intervals; Figure S4, Supporting Information) comprehensively demonstrated a well-defined lamellar structure and a spatial evolution of the geometries of the lamellae that conformed to the primary characteristics of a saddle-shaped surface. The animations in Videos S1–S3 display the complete reconstructed model viewed from rotating directions and depth slices. Based on these tomographic data, the saddle-shaped feature of the lamellae was confirmed. In addition, the four continuously fluctuating curves (marked by yellow dashed line in Figure S3, Supporting Information) clearly indicated the presence of regular triple-silts within each primary lamellar wall.

The Gaussian and mean curvatures of the saddle-shaped lamellar structure were then calculated according to the tomographic reconstruction data. A refined segmentation of the tomogram was extracted through the 3D Slicer image processing platform based on the region-growing algorithm. This process extracted the voxel data ($98 \times 109 \times 47$ nm^3) and isolated a single lamella for detailed observation and analysis (Figure 2e). Subsequently, point cloud extraction and surface fitting were performed using MATLAB (Figure 2f). The fitted surface equation of the extracted saddle-shaped lamella is expressed as following equation:

$$z = 24.91 - 3.295x - 0.9579y + 0.7066x^2 - 7.325xy - 0.3661y^2 + 0.4728x^2y + 0.5646xy^2 + 0.2984y^3 \quad (1)$$

with a mean squared error (MSE) of 1.2333. Computational analysis revealed that the surface exhibits Gaussian curvature values ($\boldsymbol{K}$) ranging from -5.41×10^{-4} to 0.41×10^{-4} nm^{-2} (Figure 2g) and mean curvature values ($\boldsymbol{H}$) spanning from -0.65×10^{-2} to 1.06×10^{-2} nm^{-1} (Figure 2h). The distributions of both $\boldsymbol{K}$ and $\boldsymbol{H}$ were depicted in Figure 2g,h with gradient colors rendering their values. The $\boldsymbol{K}$ distribution displayed negative values across 98% of the entire surface (Figure 2g$_3$), where the central region of the saddle-shaped structure exhibited the lowest Gaussian curvature, thereby quantitatively confirming the hyperbolic geometrical characteristics (Figure 2g$_1$,g$_2$). On the other hand, the $\boldsymbol{H}$ fluctuated around zero throughout the entire surface, with minimum absolute values ($\boldsymbol{H} = 0$) along asymptotic directions (marked by blue dotted line in Figure 2h$_2$), and positive and negative extrema along the principal curvature directions (marked by gray dotted line in Figure 2h$_2$), which is the typical $\boldsymbol{H}$ distribution of a saddle-shaped surface with mathematical minimal surface feature with opposite signs of $\boldsymbol{H}$ (Figure 2h). Regarding this, the typical $\boldsymbol{K}$ and $\boldsymbol{H}$ distributions of the lamellar structure reflect intermediate geometric characteristics between those of the true lamellar structure ($\boldsymbol{K} = 0$) and the complete bicontinuous structure ($\boldsymbol{K} < 0$). Then, based on the half-lamellar spacing of the saddle-shaped lamellar phase as the critical length l_c (we estimated $l_c \approx d/2 \approx 3.25$ nm, where d is the diameter of the large lamellar pores) of the hydrophobic tail, the experimental p parameter was calculated using the $\boldsymbol{K}$ and $\boldsymbol{H}$ through equation:[2]

$$p = 1 + Hl_c - 1/3Kl_c^2 \quad (2)$$

The calculated p values range from 0.978 to 1.034 (Figure S5, Supporting Information), which exceeds the spontaneous surfactant parameter of ideal bicontinuous cubic structures (≈2/3) and being close to that of an ideal bilayer structure (≈1). This increase in p parameter can be attributed to the incorporation of STAB molecules into the PAA segment that increases the Δa that contributes to the effective head group area.[17] Collectively, those Gaussian and mean curvatures and p parameter analyses provide

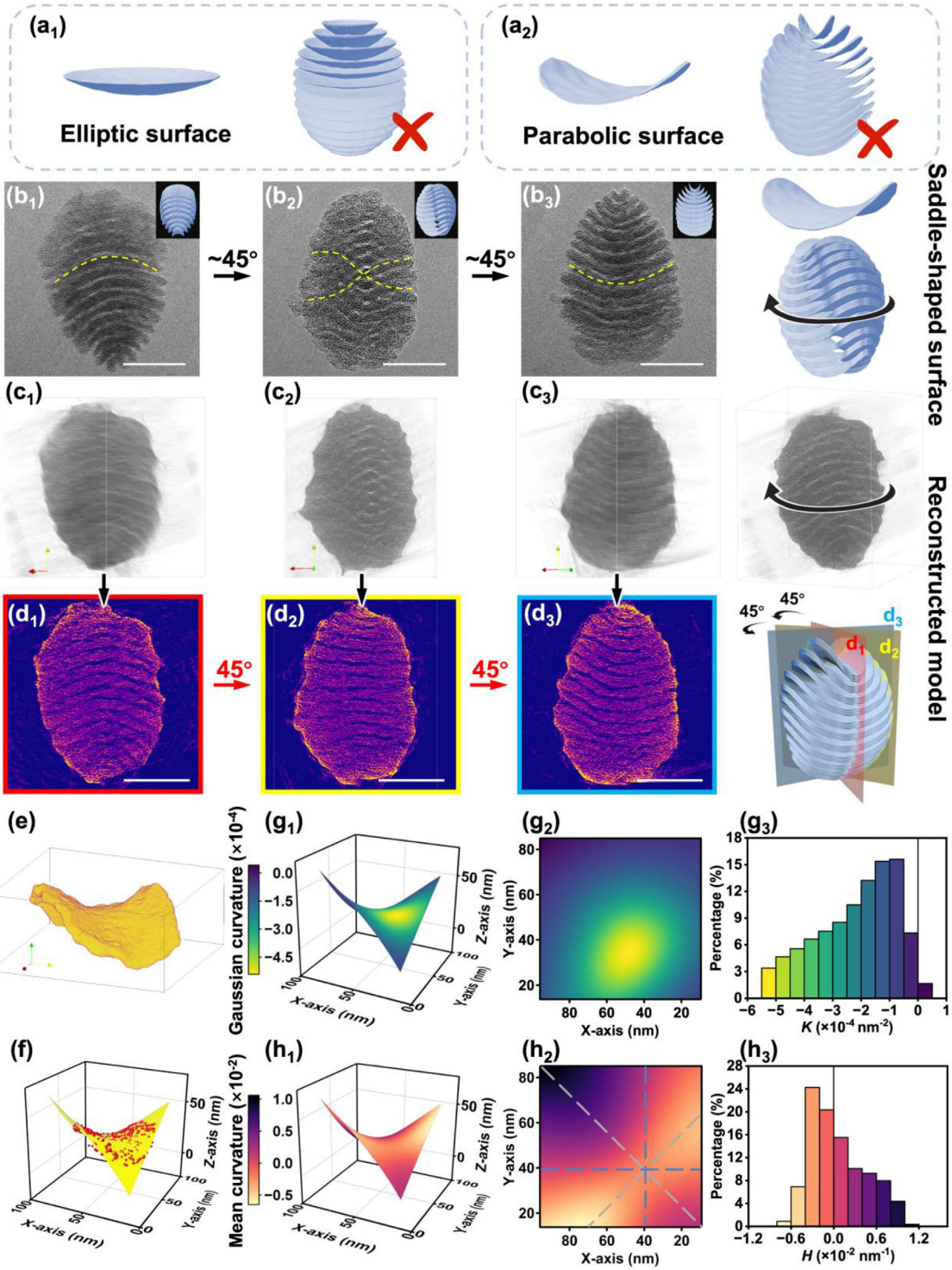

Figure 2. a_1) Model of the saddle-SML nanoparticles containing elliptic lamellae a_2) Model of the saddle-SML nanoparticles containing parabolic lamellae. b_1–b_3) TEM images of the saddle-SML obtained in synthesis conditions with molar ratio of STAB/PS_{92}-*b*-PAA_{16}/TEOS equals to 382.2:4.6:720.0. observed from different tilting directions along the long axis of the pupa-like nanoparticles and the corresponding saddle-shaped lamellar structure model indicating the tilting directions. The yellow dotted lines in each TEM image indicate the curving directions of the lamellae. Scale bar = 100 nm. c_1–c_3) Different viewpoints of the reconstruction model generated from the 2D TEM image series, the directions of the viewpoints are coincident with that in b_1–b_3. d_1–d_3) The corresponding central longitudinal sections obtained from different cross-section directions of the reconstructed model. The central longitudinal sections relative to the reconstructed model are illustrated on the right. Scale bar = 100 nm. e) The single lamella segmented from the reconstructed model. f) The point cloud extracted from the single lamella and the corresponding fitting surface. g_1–g_3) and h_1–h_3). The color-coded distributions of ***K*** and ***H*** on the saddle surface (g_1,h_1), their corresponding planar projections (g_2,h_2), and histograms (g_3,h_3) of the ***K*** and ***H***, respectively.

strong evidence for the saddle-shape lamellar structural properties of the nanoparticles. In addition, the ***K*** and ***H*** analysis derived from the 3D reconstructions of other four particles (shown in Figure S6 and Table S1, Supporting Information) confirms the high reproducibility of the structures.

Moreover, in order to eliminate the influence of kinetic transient and confirm the thermostability of the saddle-shaped lamellar structure, we supplemented a series of TEM observations on the organic composite micelles during different aging times prior to silicification (Figure S7, Supporting Information) and on the silica samples collected at different stages during the silicification process (Figure S8, Supporting Information). It can be shown that both the composite micelles and the silica nanoparticles exhibited the typical contrast of the saddle shaped lamellas at the initial aging time (0 min), and those structures were maintained during different aging time. This finding excludes the influence of kinetic effects in the assembly process and the effect of the inorganic precursor on the final structure, confirming the thermodynamically stability of the saddle-shaped lamellar structure.

2.3. Structural Modulation and Mechanism Exploration of Saddle-SML

The intermediate state connecting the lamellar and the bicontinuous hyperbolic cubic phase implies that the formation mechanism of the saddle-shaped lamellar structure would be highly related to the lamellar-bicontinuous phase transition problems.

Given that the structural modulator STAB plays a critical role in the binary system, we started the mechanism exploration by investigating the effect of STAB on the formation of the complex mesostructures through adjusting the ratio between STAB and PS_{92}-*b*-PAA_{16} (**Figure 3a**). The increasing content of STAB induced an obvious structural transition trend from mono-subpore lamella to multi-subpores (marked by short lines with different colors) lamella then to the lamellar/bicontinuous mixture phase (the bicontinuous phase is marked by green arrows). The SAXS patterns of all samples are shown in Figure S9 (Supporting Information). The appearance of a shoulder peak at q = 0.046 $Å^{-1}$ at higher STAB contents suggests a structural change from lamellar into bicontinuous phase (marked by blue triangles in Figure S9, Supporting Information). With a low content of STAB (STAB/PS_{92}-*b*-PAA_{16} molar ratio of 254.8:4.6, mass ratio of 100:50), only unclear and patchy **mono-subpore** or **di-subpores** were observed (Figure $3a_1$). The lamellae of each particle extended to uniform **tri-subpores** with regular edges when the STAB/PS_{92}-*b*-PAA_{16} molar ratio increases to 382.2:4.6 (mass ratio of 150:50) (Figure $3a_2$) and this **tri-subpores** also appeared at higher STAB contents. However, the higher STAB amounts led to the phase transformation from saddle-shaped lamellae to bicontinuous mesostructures. The **tri-subpores** lamellar phase and the bicontinuous phase coexisted when the STAB/PS_{92}-*b*-PAA_{16} molar ratio was increased to 509.6:4.6 and 636.9:4.6 (mass ratio of 200:50 and 250:50, Figure 3a3,a4). When the STAB/PS_{92}-*b*-PAA_{16} molar ratio was increased to 764.3:4.6 (mass ratio of 300:50), the lamellar structure reverted to **mono-subpores** accompanied by the formation of a dense solid outer-shell with radial epitaxial channels extending from the internal lamellae (highlighted by the red arrows in the inserted picture in Figure S10a, Supporting Information) and the bicontinuous phase transformed into a typical cubic gyroid (G) structure (marked by the yellow arrows in Figure S10a, Supporting Information). However, excessively high STAB amounts (the STAB/PS_{92}-*b*-PAA_{16} molar ratio of 1019.1:4.6 and the mass ratio of 400:50, Figure S10b, Supporting Information) led to the formation of irregular micron particles due to the collapse of the ordered co-assembly system under too strong electrostatic shielding effect of the surfactants to the block copolymers. Only a minor fraction of ordered phases with bicontinuous features coexisted with the irregular aggregates under this condition (inset in Figure S10b, Supporting Information). The evolution of the structures was further analyzed with N_2 adsorption-desorption isotherms (Figure S11, Supporting Information). Along with the increasing of STAB concentrations, the hysteresis loops change from H1-type to H4-type, demonstrating the increasing fractions of the narrow slit-shaped mesopores, which is consistent with the TEM observations. The regulations along changing the relative contents of block copolymers exhibited similar structure transition trends (Figure S12, Supporting Information). The reduction in the relative proportions of PS_{92}-*b*-PAA_{16} (with a concomitant relative increase in STAB ratio) induced a rise-and-decline trends in the number of subpores per primary lamellar wall, indicating that an optimal surfactant/block copolymer molar ratio range from 68.83 to 137.66 would induce the most hierarchical tri-subpores.

The interfacial curvature of a block polymer at the hydrophilic/hydrophobic interface is determined by the molecular dimensions, such as the volume fraction of the blocks, which then plays a critical role in defining the structural features of their aggregates. Therefore, to modulate the interfacial curvature, we engineered a series of PS_x-*b*-PAA_y diblock copolymers (namely, the PS_{54}-*b*-PAA_{16}, PS_{68}-*b*-PAA_{21}, and PS_{109}-*b*-PAA_{16}, Figures S13–S15 and Table S2, Supporting Information) and systematically investigated the phase behaviors of their binary systems with STAB. Collectively, all the systems of PS_x-*b*-PAA_y underwent a lamellar-to-bicontinuous phase transformation with increasing STAB/PS_x-*b*-PAA_y molar ratio. It was found that the PS segments showed a limited role in influencing the subpore structures, but have a more substantial effect on the phase transition from lamellae to bicontinuous phase. For the PS_{54}-*b*-PAA_{16} with the shortest PS chains, lamellae of pupa-like nanoparticles with **mono-subpores** and sporadically dispersed **di-subpore** pupa-like nanoparticles were observed (Figure 3b), while a substantial fraction of bicontinuous phase was obtained once STAB/PS_{54}-*b*-PAA_{16} molar ratios reached 382.2:7.4 or higher (509.6:7.4 and 636.9:7.4) (Figure 3b2–b4). With the increasing of the PS chain length, a transition from mono- to hierarchical-subpores structures occurred and the lamellar-to-bicontinuous phase transformation occurred only at higher STAB contents, as shown in the TEM images of the PS_{68}-*b*-PAA_{21} (Figure 3c), PS_{92}-*b*-PAA_{16} (Figure 3a) and PS_{109}-*b*-PAA_{16} (Figure 3d). Notably, when the PS chain increased to 109 (PS_{109}-*b*-PAA_{16}), the **tri-subpores** were mainly identified (Figure 3d). In contrast, the variations in PAA chain had a more pronounced influence on the lamellar structures. The larger the volume of the PAA segments, the more subpores within one primary lamellar wall. Longer PAA segments, such as that in PS_{68}-*b*-PAA_{21}, led to a lamellar structure with at least **quadruple-subpores** even under the low STAB/PS_{68}-*b*-PAA_{21} molar ratio of 382.2:5.8 and 509.6:5.8 (mass ratio of 150:50

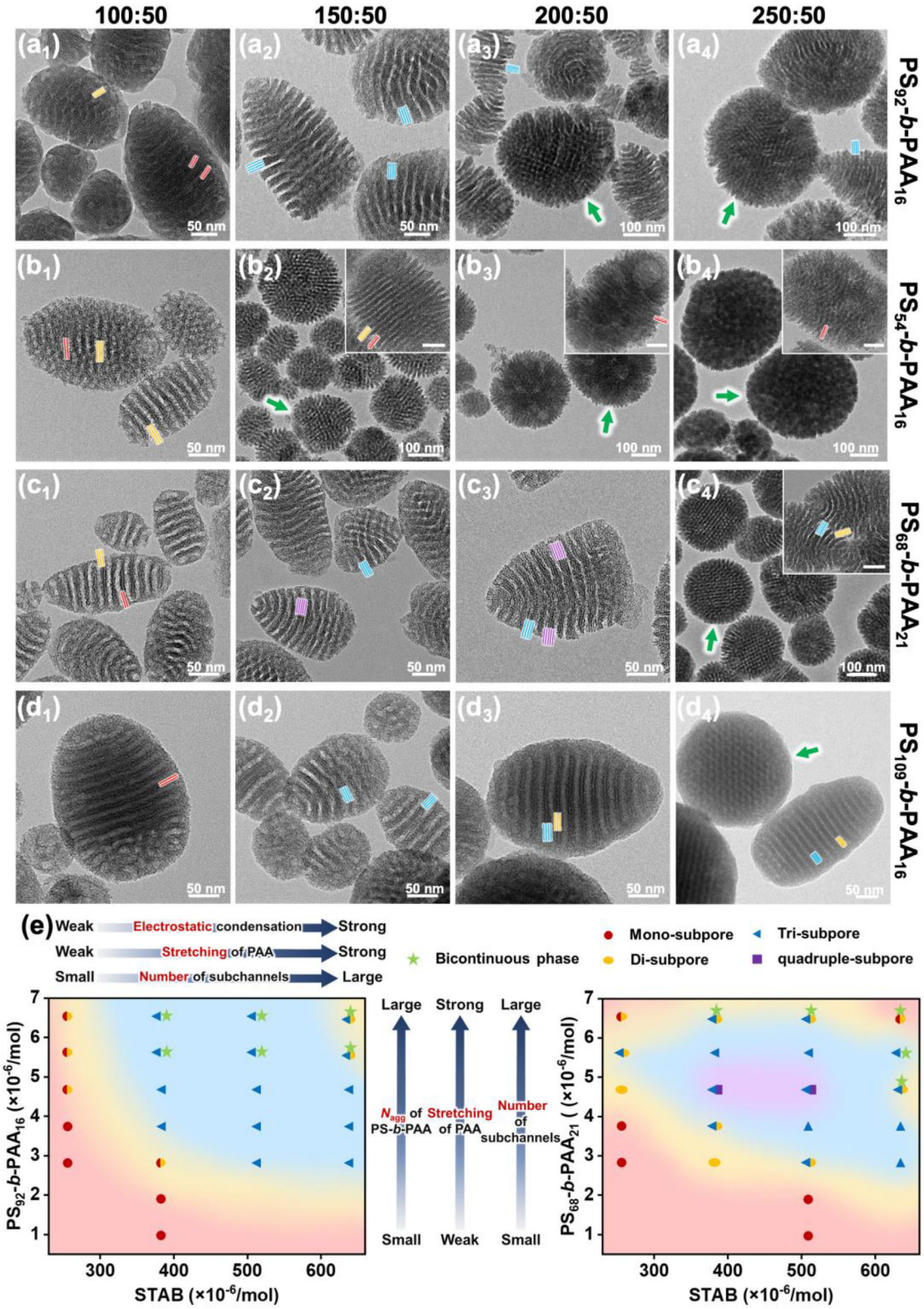

Figure 3. TEM images of the sample series obtained by adjusting the concentration of STAB and the synthesis-field diagram with different PS_x-*b*-PAA_y. a) The STAB/PS_{92}-*b*-PAA_{16} molar ratios are 254.8:4.6, 382.2:4.6, 509.6:4.6, and 636.9:4.6. b) The STAB/PS_{54}-*b*-PAA_{16} molar ratios are 254.8:7.4, 382.2:7.4, 509.6:7.4, and 636.9:7.4. c) The STAB/PS_{68}-*b*-PAA_{21} molar ratios are 254.8:5.8, 382.2:5.8, 509.6:5.8, and 636.9:5.8. d) The STAB/PS_{109}-*b*-PAA_{16} molar ratios are 254.8:4.0, 382.2:4.0, 509.6:4.0, and 636.9:4.0. e) Synthesis-field diagram of PS_{92}-*b*-PAA_{16} and PS_{68}-*b*-PAA_{21}. The scale bars of all inset images are 50 nm.

and 200:50, Figure 3c$_2$,c$_3$). However, limited by the saturation thresholds of electrostatic saturation and volumetric capacity in hydrophilic segments, and the occurrence of phase transition, the subpores reached an upper limitation of quadruple-pores.

Therefore, according to all the TEM observations (Figures S16 and S17, Supporting Information) of samples obtained by the systematic modulation of PS_{92}-*b*-PAA_{16} and PS_{68}-*b*-PAA_{21}, a series of synthesis-field diagrams (Figure 3e) was depicted. Obviously, it could be found that in a suitable range of STAB/PS_x-*b*-PAA_y molar ratios, increasing the contents of both copolymer and surfactant enhanced the number of subpores and eventually promoted the transformation of the systems from lamellar into the cubic bicontinuous phase. When we maintained the concentration of PS_x-*b*-PAA_y, under low STAB content, the STAB micelles only formed loose, mono-subpore assemblies (corresponding to the mono-subpore in saddle-SML). Increasing STAB content enhanced STAB micelle adsorption and enrichment in PAA regions, inducing orderly dense packing of STAB micelles, and finally to the 3D bicontinuous phase. This promoted conformational extension of PAA chains and formed higher-level assemblies (exhibiting multi-subpores). Conversely, under fixed STAB conditions, an elevated PS_x-*b*-PAA_y content with increasing aggregation number (N_{agg}) reduced electrostatic repulsion between PAA chains through enhanced chain extension, ultimately led to more micellar adsorption and multiplicity of subpores. These phase grams highlight the importance of the variation of the chain volume fraction in the formation of different hierarchical structures.

2.4. Discussion

Based on the above comprehensive characterizations, we could elucidate a formation mechanism of the saddle-shaped lamella by addressing two critical questions:

2.4.1. Why Does the Lamellar Structure Contain Hierarchical Subpores?

The self-assembly of the binary system occurs in the presence of a substantial amount of solvent. The incompatibility between the molecules and the solvent, along with the interactions between the polymers and the surfactants, induces a highly concentrated area for a local phase separation, followed by the formation of discrete micelles, within which confined microphase separation occurs. Therefore, those highly concentrated dispersed microdomain determined the final nanoparticle morphologies. Due to the surface tension of the solvent, the nanoparticles prefer an ellipsoidal morphology to maintain a lowest surface energy. In the final nanoparticles, the two distinct pores demonstrated the cooperative interactions between the two components of the binary system, whose spatial arrangements visually illustrated the relative positions and spatial relationships of the different assemblies (**Figure** 4a). In a binary system containing large block copolymer with anionic PAA segments and small molecule surfactant with cationic head groups, there are strong electrostatic interactions between the two components, and the STAB micelles could be absorbed and embedded into the PAA segments. The large PAA domains thus provided an electron-rich space for confining STAB micelles toward higher-level assemblies (Figure 4b). As can be inferred from the phase diagrams, the hierarchy of the subpores increased from mono-subpore to quadruple-subpore along with the increasing of STAB contents (Figure 4c,i) or the expansion of the PAA domains (Figure 4c,ii). The variations of the multi-subpores by adjusting the STAB micelles provided direct evidence for locating the positions of binary components within the composite aggregates, confirming the effective insertion of STAB micelles in the PAA segments. This molecular distribution analyze will facilitate us to further understand the intermolecular interactions and geometrical variations within composite micelles and thus understand the critical mechanism in inducing the phase transitions.

2.4.2. Why Does the Lamellar Structure Become Saddle-Like?

The inserting of STAB significantly alters the molecular geometry of PS_x-*b*-PAA_y aggregates, thereby directly modifying their assembly behaviors. As the main building block of the binary system, the spontaneously phase separation of the block copolymer driven by the PS/H_2O and the PS/PAA incompatibility in the THF/H_2O solvent are the main driving force of the hierarchical architectures. During this process, the relative volume fraction of each polymer chain defines the interfacial curvature of the polymer, which determines the aggregate phases (e.g., lamellar, bicontinuous or hexagonal phases). For example, PS_{92}-*b*-PAA_{16}, whose volume fraction of the PAA segment is 10.48%, has a wide window for generating cubic bicontinuous structures with negative Gaussian curvatures under bulk phase separation conditions.[36] In the aqueous binary assembly system, the insertion of massive STAB micelles introduces two competing effects: volumetric expansion effect and electrostatic screening effect (Figure 4d). The volumetric expansion effect tends to swell the PAA chains through molecular intercalation, thereby increasing the interchain distance between PAA molecules. However, the electrostatic screening effect in turn leads to the charge neutralization-driven contraction and densification of PAA. To balance the competitive interplay and accommodate additional molecules within confined spaces, the lamellar structure gradually fluctuate to upward convexities and downward concavities, ultimately evolves from planar lamellae into saddle-shaped lamellae with negative Gaussian curvature (Figure 4d). Meanwhile, the inherent propensity of PS_{92}-*b*-PAA_{16} to establish bicontinuous phase structures in aqueous is counterbalanced through the synergistic equilibrium between the two competing effects, thereby precisely modulating *p* value to a critical intermediate value between that of the lamellar and bicontinuous phases.

From an energetic perspective, the addition of STAB redistributes the conformational entropy of polymer chains and establishes a locally concave free energy landscape, thereby disrupting the energetic equilibrium of planar configurations and driving the system toward a thermodynamically stable saddle-shaped morphology. In our previous work, we have also captured a shifted tetragonal G intermediate phase (tG) between the lamellar phase and the cubic bicontinuous G phase in a PS_{92}-*b*-PAA_{16} binary system containing a surfactant with a shorter tail of 14 alkyl groups (C_{14}TAB) or a surfactant with 16 alkyl

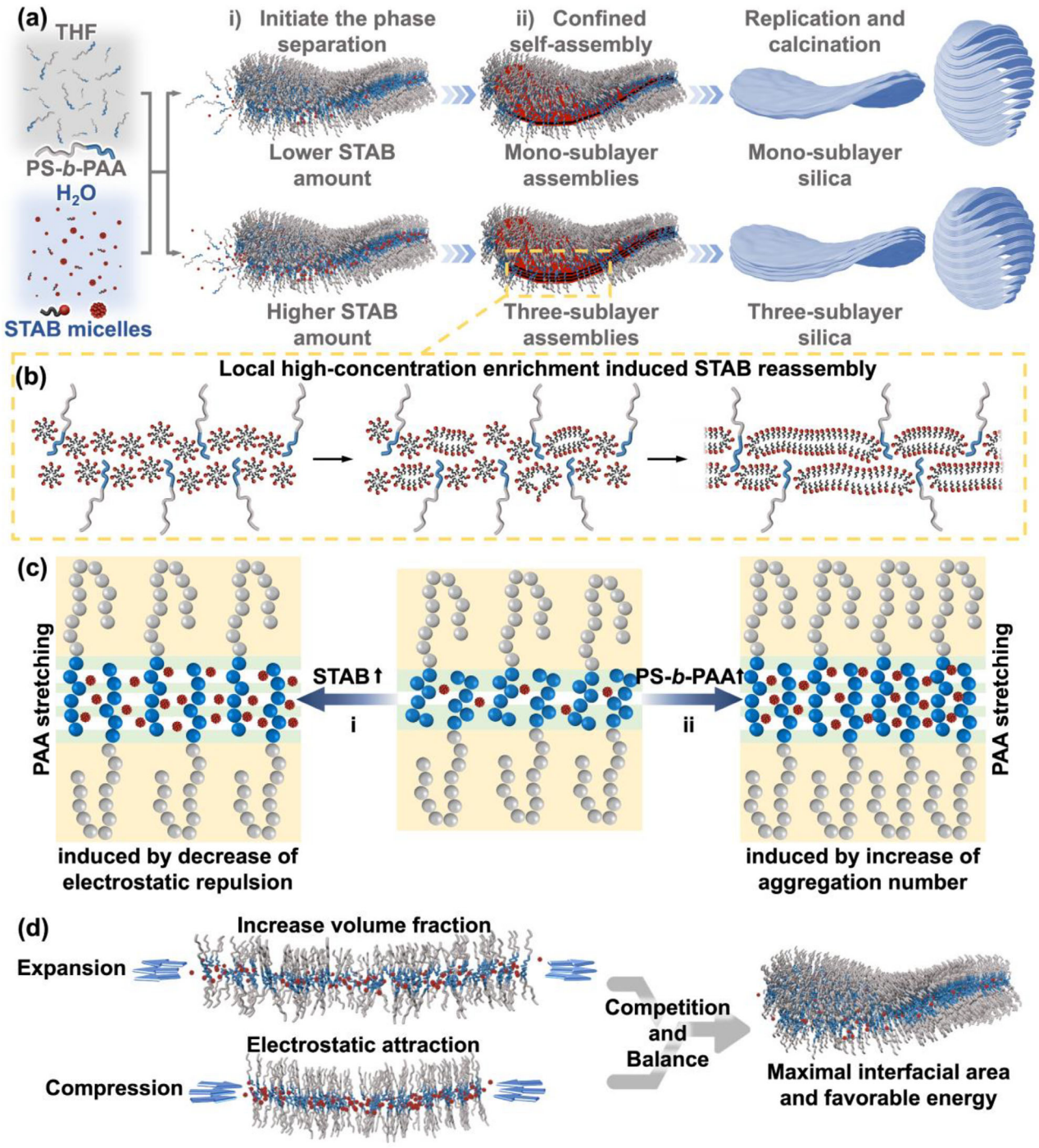

Figure 4. Schematic drawing of a) the synthetic mechanism of the formation of the hierarchical saddle-shaped lamellar structure with varying STAB amounts. b) The magnified interacting illustration indicates the assembly of STAB micelles within the electron-rich PAA domains. c) The influence of the varying STAB and PS_x-*b*-PAA_y contents on the molecular arrangements. d) The schematic diagram of the saddle-shaped structure formed by the competition and balance between the electrostatic screening and volume expansion effects.

groups (C_{16}TAB).[30] No lamellar structure had been obtained in the C_{14}TAB/PS_{92}-*b*-PAA_{16} system during the disorder to cubic phase transition process, while the structures in C_{16}TAB/ PS_{92}-*b*-PAA_{16} system transited from a loose lamellar phase to the lamellar/cubic intergrown structure then to the tG and cubic G phases, and the lamellar phase has occupied a large phase region in the STAB (i.e., C_{18}TAB)/PS_{92}-*b*-PAA_{16} system. For pure surfactants, along with the elongation of the alky chains, the surfactants exhibit increased *p* parameter thus prefer forming micelles with lower interfacial curvature (i.e., toward lamellar structures). This

propensity greatly influenced the shapes of the surfactants aggregates locally assembled within the electron-rich PAA domains. Meanwhile, the geometrical matching between the preferred surfactant aggregates and the final composite C_xTAB/PS_{92}-*b*-PAA_{16} aggregates would highly promote the stability of the binary system. Therefore, we could see that the interfacial curvature of the binary composite micelles changed coincident with the shape of the surfactants, a phenomenon we defined as the *interfacial curvature matching* effect. Thus, from both the geometric matching and interaction locking aspects, this *interfacial curvature matching* effect along with the competing interactions stabilize the saddle-shaped intermediate phase that is elusive in conventional phase diagrams.

As a consequence, the interaction between PS_x-*b*-PAA_y and STAB along with their *interfacial curvature matching* effect, are crucial for the formation of such delicate hierarchical structures. The complex volume effects and electrostatic interactions between the two components are the key for the formation of a saddle-shaped surface, which—through interfacial curvature modulation—achieves enhanced molecular accommodation capacity within confined spaces and optimized energy state. The thermostability of the saddle-shaped lamellar phase confirmed the existence of the intermediate phase between the planar lamellar and hyperbolic bicontiunous phases, implying the existence of the smooth lamellar-bicontinuous phase transition pathway.

3. Conclusion

In summary, saddle-shaped hierarchical lamellar mesostructures with typical negative Gaussian curvatures have been constructed in a binary co-assembly system containing large block copolymer and small molecule surfactant. The precisely manipulated molecular interactions between the two components allow a complex cooperative assembly behavior that induces the formation of exceptional phases rarely observed in traditional single-component assembly systems. STAB promotes the rearrangement of PAA chains and redistributes its conformational entropy, whereas the PAA segments provide an electron-rich space to confine a high-level assembly of STAB micelles. The competition between the volumetric expansion effect and electrostatic screening effect of the inserted STAB micelles on the polymer volume eventually achieve self-adaptive interfacial curvature matching and energy minimization, resulting in the formation of a saddle-shaped hierarchical lamellar structure with more densely packed polymers in confined lamellae. The discovery of the unusual phase within the binary system proved that there indeed an intermediate phase with an exceptional negative Gaussian curvature between the planar lamellar and hyperbolic bicontinuous phases, which confirmed the existence of the smooth lamellar-bicontinuous phase transition process. This discovery may play a decisive role in revealing evolution of different curvatures during the dynamic phase transitions, particularly providing novel referable substantiated evidence for understanding the membrane transfer in complex biological architectures such as biomembrane systems. In addition, this finding also highlights the potential of the binary system in obtaining specific structures that outside the traditional phases of pure block copolymer phase separation, providing a new perspective to realize the customization design and optimization of mesoscopic structures.

4. Experimental Section

Materials: Tetraethyl orthosilicate (TEOS, equivalent SiO_2, R28%) and toluene (R99.5%) were purchased from Sinopharm Chemical Reagent. The ammonia solution (25%–28%), tetrahydrofuran (THF, R99.5%), dichloromethane (DCM, R99.5%), methanol (R99.5%), trifluoroacetic acid (TFA, R99%), and ethanol (R99.8%) were obtained from Shanghai Titan Scientific, stearyltrimethylammonium bromide (STAB, R98%), and cuprous bromide (CuBr, R99%) were purchased from Aladdin Holdings Group. Methyl 2-bromopropionate (MBP, R98%), N,N,N′,N′,N″-pentamethyldiethylenetriamine (PMDETA, R99%), t-butyl acrylate (t-BA, R98.0%), and styrene (St, R99.0%) were purchased from Tixaid (Shanghai) Chemical Industry Development. Water was purified with a Milli-Q system and had an electrical resistance of 18.2 MΩ·cm^{-1}. t-BA and St were purified by filtration through an Al_2O_3 column for removal of the polymerization inhibitor.

Synthesis of the Block Copolymer PS_x-b-PAA_y—Synthesis of $PtBA_y$-Br: The macroinitiator $PtBA_y$-Br was synthesized by using the well-established atom transfer radical polymerization (ATRP) technique with *t*-Butyl acrylate (*t*-BA) at 60 °C, using methyl 2-bromopropionate (MBP) as the initiator and cuprous bromide/*N*,*N*,*N*′,*N*′,*N*″-pentamethyldiethylenetriamine (CuBr/PMDETA) as the catalyst system. Typically, MBP (0.308 mol, 5.150 g) was dissolved in toluene (97 mL) in a 250 mL Schlenk flask, and *t*-BA (0.400 mol, 58 mL), PMDETA (0.308 mol, 6.41 mL), and CuBr (0.308 mol, 4.418 g) were added to the solution. The reaction system was fully degassed with more than three freeze–pump–thaw cycles and sealed under vacuum. The bottle was then placed in an oil bath at 60 °C for 4 h to allow polymerization to occur. After terminating the polymerization by exposing the reaction mixture to air, the catalyst was removed with filtration through an Al_2O_3 column using methylene chloride as eluent. After rotary evaporation to remove the methylene chloride and toluene, the macroinitiator $PtBA_{16}$-Br was obtained. The synthesis of the macroinitiator $PtBA_{21}$-Br was carried out only by modulating the amount of *t*-BA (0.463 mol, 67 mL), while keeping other conditions constant.

Synthesis of the Block Copolymer PS_x-b-PAA_y—Synthesis of PS_x-b-$PtBA_y$: PS_x-*b*-$PtBA_y$ was synthesized by ATRP of St at 90 °C using $PtBA_y$-Br as the initiator and CuBr/PMEDTA as the catalyst system. For a typical synthesis, a 250 mL Schlenk flask containing $PtBA_{16}$-Br (4.31 mmol, 9.0 g), PMDETA (8.61 mmol, 1.79 mL), toluene (65 mL), and St (0.557 mol, 64.0 mL) was purged thoroughly and then sealed with a rubber stopper. After the solution became clear with stirring in an ice-water bath, CuBr (4.31 mmol, 0.63 g) was added to the solution. The bottle containing the reactants was fully degassed with more than three freeze–pump–thaw cycles and sealed under vacuum. The flask was then placed in an oil bath at 90 °C to allow polymerization. The reaction time was controlled at 6 h. After the reaction, as with the synthesis of $PtBA_{16}$-Br, the mixtures were cooled to room temperature, the catalyst was removed, and the block copolymer PS_{92}-*b*-$PtBA_{16}$ was finally obtained by precipitation with cold methanol (500 mL) after rotary evaporation. The block copolymer PS_{54}-*b*-$PtBA_{16}$ and PS_{109}-*b*-$PtBA_{16}$ were synthesized by changing the amount of St (0.431 mol, 49.5 mL) and the reaction time (6 h), respectively. The block copolymer PS_{68}-*b*-$PtBA_{21}$ was synthesized by ATRP of St (0.450 mol, 51.7 mL) for 5 h using $PtBA_{21}$-Br (3.46 mmol, 9.0 g) as the initiator.

Synthesis of the Block Copolymer PS_x-b-PAA_y—Synthesis of PS_x-b-PAA_y: The amphiphilic copolymer PS_x-*b*-PAA_y was hydrolyzed from PS_x-*b*-$PtBA_y$. PS_x-*b*-$PtBA_y$ (20.0 g) was dissolved in DCM (150 mL) in a 250 mL beaker, and then 58.6 mL of trifluoroacetic acid (0.79 mol) was added to the mixture. The reaction was stirred at room temperature for three days. After rotary evaporation to remove most of the DCM, the concentrate was added to cold methanol to precipitate the PS_x-*b*-PAA_y diblock copolymer, which was collected by filtration and dried under vacuum at room temperature.

Fabrication of the Saddle-SML Composite Micelles: Typically, a copolymer solution (solution A) was prepared by dissolving block copolymer PS_x-*b*-PAA_y (x mg, x = 10, 20, 30, 40, 50, 60, and 70) in THF (10 mL), and surfactant solution (solution B) was prepared by dissolving the surfactant STAB (x mg, x = 100, 150, 200, 250, 300, and 400) and ammonia (500 µL) in deionized water (40 mL). All solutions were kept in a 35 °C water bath. Then, solution A was quickly poured into solution B with constant

magnetic stirring at 700 rpm and stirred for another 2–3 s. The milky white composite micelle solution was obtained. The micellar nanoparticles were collected by centrifuging the final solution at 17940 × g for 10 min and washed with purified water and ethanol alternately for at least two times.

Fabrication of the Saddle-SML Silica Nanoparticles: Inorganic precursor solution was prepared by dropwise adding TEOS (0.72 mmol, 0.3 g) into ethanol (80 mL). Then the as-made organic micellar nanoparticles solution was poured into the inorganic precursor solution at a constant speed with constant stirring at 400 rpm for 10 min. The reaction solution was then aged for 18 h. The as-synthesized nanoparticles were collected by centrifugation at 17940 × g for 10 min, washed with purified water and ethanol alternately for at least two times, and dried in a vacuum oven at 35 °C for 12 h. Template-free samples were obtained by calcination of the as-made samples at 550 °C for 6 h with heating rate of 1 °C·min^{-1}.

Electron Tomography (ET) of the Saddle-SML Silica Nanoparticles: For ET, the samples were crushed, dispersed in ethanol, and dripped on a carbon thin film on a Cu grid. A series of bright-field micrographs was acquired at tilt angles in the range of ±60° at an angular interval of 5°. Image alignment, reconstructions, and visualization were then performed using MATLAB and tomviz. The 3D volume reconstruction was achieved by real-space iterative reconstruction (RESIRE) algorithm.

Isolation and Calculation of Gaussian and Mean Curvatures of the Single Lamella: Surface extraction was performed by processing the reconstructed model in 3D Slicer to isolate single-lamella voxels. After smoothing in MATLAB, median points of opposing surfaces were derived, yielding the point clouds. Point cloud surface fitting was implemented in MATLAB using the fit function with a polynomial model (poly23). Following surface fitting, the ComputeCurvature function is employed to calculate both Gaussian curvature and mean curvature at grid points with unit spacing (step = 1) across the fitted surface.

Characterizations: The nitrogen adsorption–desorption experiment was performed using Quantachrome Instruments Autosorb iQ at 77 K. All of the samples were degassed under vacuum at 100 °C for 6 h prior to analysis. For TEM observations, the samples were crushed, dispersed in ethanol and dripped on a carbon thin film on a Cu grid. The 2D TEM experiments were performed using a JEOL JEM-2100 microscope (JEOL, Ltd., Japan). ET was carried out using a JEM-F200 microscope (JEOL, Ltd., Japan) operated at 200 kV, and the images were recorded with a GATAN Oneview IS camera under low-dose conditions. SAXS patterns were obtained on a Rigaku NANOPIX system. The X-ray generator was Fr-x (rotation anode X-ray generator) with a power of 2.97 kW (45 kV, 66 mA), and the λ for the target Cu source was 1.5406 Å. The camera length was 1290 mm. The incident beam was from New CMF optics, and the detector was a Hy-Pix-54000. All ID profiles were collected with two-pinhole, high-resolution-type collimation with a beam stop size of 2.0 mmφ. Before measurements, the camera length was calibrated with silver behenate. The NMR spectra were recorded via a Bruker Avance 600 MHz NMR spectrometer using tetramethylsilane (TMS) as the internal reference. Gel permeation chromatography (GPC) was recorded by Waters1515 gel permeation chromatography with THF as the mobile phase.

Supporting Information

Supporting Information is available from the Wiley Online Library or from the author.

Acknowledgements

The authors thank Prof. Hexiang Deng and Dr. Gaoli Hu (Wuhan University) for the support for SAXS measurements, and Dr. Xueliang Zhang (Tongji University) for the help in ET reconstruction. This work was financially supported by the National Key Research and Development Program of China (2022YFC2403200), the National Natural Science Foundation of China (22472058 and 22425303), Shanghai Pilot Program for Basic Research (22TQ1400100-13), the Fundamental Research Funds for the Central Universities.

Conflict of Interest

The authors declare no conflict of interest.

Data Availability Statement

The data that support the findings of this study are available from the corresponding author upon reasonable request.

Keywords

bicontinuous cubic phase, Gaussian curvature, lamellar phase, mean curvature, structural transition

Received: July 5, 2025
Revised: November 26, 2025
Published online:

[1] B. O'Neill, *Elementary Differential Geometry*, 2nd ed., Elsevier, Amsterdam **2006**.
[2] C. F. Gauss, *Disquisitiones Generales Circa Superficies Curvas*, Verlag Dieterich, Mainz **1828**.
[3] S. Hyde, Z. Blum, T. Landh, S. Lidin, B. W. Ninham, S. Andersson, K. Larsson, *The Language of Shape: the Role of Curvature in Condensed Matter: Physics, Chemistry and Biology*, Elsevier, Amsterdam **1996**.
[4] J. Stillwell, *Sources of Hyperbolic Geometry*, American Mathematical Society, Providence **1996**.
[5] C. R. Calladine, *Theory of Shell Structures*, Cambridge University Press, Cambridge **1983**.
[6] X. Xu, Q. Zhang, M. Hao, Y. Hu, Z. Lin, L. Peng, T. Wang, X. Ren, C. Wang, Z. Zhao, C. Wan, H. Fei, L. Wang, J. Zhu, H. Sun, W. Chen, T. Du, B. Deng, G. J. Cheng, I. Shakir, C. Dames, T. S. Fisher, X. Zhang, H. Li, Y. Huang, X. Duan, *Science* **2019**, *363*, 723.
[7] Z. Xu, T. Xiao, Y. Li, Y. Pan, C. Li, P. Liu, Q. Xu, F. Tian, L. Wu, F. Xu, Y. Mai, *Adv. Mater.* **2025**, *37*, 2416204.
[8] H. Y. Hsueh, H. Y. Chen, M. S. She, C. K. Chen, R. M. Ho, S. J. Gwo, H. Hasegawa, L. Edwin, *Nano Lett.* **2010**, *10*, 4994.
[9] E. Goi, B. P. Cumming, M. Gu, *Adv. Opt. Mater.* **2018**, *6*, 1800485.
[10] C. Wang, C. C. Cui, Q. Z. Deng, C. Zhang, S. S. Asahina, Y. Y. Cao, Y. Y. Mai, S. A. Che, L. Han, *Proc. Natl. Acad. Sci. U.S.A.* **2024**, *121*, 2318072121.
[11] Y. Kozlovsky, M. M. Kozlov, *Biophys. J.* **2003**, *85*, 85.
[12] Y. Deng, M. Mieczkowski, *Protoplasma* **1998**, *203*, 16.
[13] S. Andersson, S. T. Hyde, V. H. G. Schnering, *Z. Krist. - Cryst. Mater* **1984**, *168*, https://doi.org/10.1524/zkri.1984.168.14.1.
[14] A. L. Mackay, H. Terrones, *Nature* **1991**, *352*, 762.
[15] C. V. Kulkarni, *Chem. Phys. Lipids* **2019**, *218*, 16.
[16] J. N. Israelachvili, D. J. Mitchell, B. W. Ninham, *J. Chem. Soc., Faraday Trans. 2* **1976**, *72*, 1525.
[17] S. T. Hyde, I. S. Barnes, B. W. Ninham, *Langmuir* **1990**, *6*, 1055.
[18] Y. Y. Mai, A. Eisenberg, *Chem. Soc. Rev.* **2012**, *41*, 5969.
[19] M. V. Voinova, in *Statistical Mechanics of Biocomplexity* (Eds: D. Reguera, J. Vilar, J. Rubí), Springer, Berlin **2007**, pp. 38–45.
[20] W. Helfrich, *Z. Naturforsch. C* **1973**, *28*, 693.
[21] T. Zhan, W. H. Lv, Y. R. Deng, *Protoplasma* **2017**, *254*, 1923.
[22] B. G. Tenchov, R. C. MacDonald, D. P. Siegel, *Biophys. J.* **2006**, *91*, 2508.
[23] R. Koynova, B. Tenchov, *Recent Pat. Drug Deliv. Formul.* **2013**, *7*, 165.
[24] J. Barauskas, M. Johnsson, F. Joabsson, F. Tiberg, *Langmuir* **2005**, *21*, 2569.
[25] Y. Zhang, O. Y. Cohen, M. Moshe, E. Sharon, *Scienc* **2025**, *388*, 520.

[26] L. Han, S. Che, *Adv. Mater.* **2018**, *30*, 1705708.
[27] Y. Yu, L. Zhang, A. Eisenberg, *Macromolecules* **1998**, *31*, 1144.
[28] E. G. Kelley, T. P. Smart, A. J. Jackson, M. O. Sullivan, T. H. Epps, *Soft Matter* **2011**, *7*, 7094.
[29] Q. Sheng, H. Chen, W. Mao, C. Cui, S. Che, L. Han, *Angew. Chem., Int. Ed.* **2021**, *60*, 15236.
[30] S. Q. Wang, H. Chen, T. Y. Zhong, Q. Z. Deng, S. B. Yang, Y. Y. Cao, Y. S. Li, L. Han, *Chem* **2024**, *10*, 1406.
[31] K. H. Ku, J. M. Shin, H. Yun, G. R. Yi, S. G. Jang, B. J. Kim, *Adv. Funct. Mater.* **2018**, *28*, 1802961.
[32] D. J. De Rosier, A. Klug, *Nature* **1968**, *217*, 130.
[33] W. Baumeister, R. Grimm, J. Walz, *Trends Cell Biol.* **1999**, *9*, 81.
[34] Y. Yang, J. Zhou, F. Zhu, Y. K. Yuan, D. J. Chang, D. S. Kim, M. Pham, A. Rana, X. Z. Tian, Y. G. Yao, *Nature* **2021**, *592*, 60.
[35] M. Pham, Y. Yuan, A. Rana, S. Osher, J. Miao, *Sci. Rep.* **2023**, *13*, 5624.
[36] M. Stefik, S. Mahajan, H. Sai, T. H. Epps III, F. S. Bates, S. M. Gruner, F. J. DiSalvo, *Chem. Mater.* **2009**, *21*, 5466.